

Utilization of the k -Space Method in the Design of a Ferroelectric Hyperthermia Phased Array

OSAMA M. AL-BATAINEH,¹ T. DOUGLAS MAST,²
EUN-JOO PARK,^{1,*} VICTOR W. SPARROW,³
ROBERT M. KEOLIAN,^{3,4} AND NADINE BARRIE SMITH^{1,3}

¹Department of Bioengineering, The Pennsylvania State University,
University Park, PA 16802

²Department of Biomedical Engineering, University of Cincinnati, Cincinnati,
OH 45267

³Graduate Program in Acoustics, The Pennsylvania State University,
University Park, PA 16802

⁴Applied Research Laboratory, The Pennsylvania State University,
University Park, PA 16802

This research utilizes the k -space computational method and a three-dimensional (3D), inhomogeneous, large scale, and coarse grid human prostate model to design and to fabricate an intracavitary probe for hyperthermia treatment of prostate cancer. A 3D acoustical prostate model was created utilizing photographic data from the Visible Human Project[®]. Ultrasound wave propagation of the designed phased array was simulated by means of the k -space computational method. Four stacked linear phased arrays composed the 80 elements hyperthermia array. Good agreement between the dosimetry and the k -space simulation results was obtained. As an example, the measured -3 dB distance of the focal volume in the propagation direction deviated by only 9% compared to simulated results.

Keywords k -space; hyperthermia; ultrasound; prostate cancer; therapeutic

1. Introduction

Prostate cancer causes approximately 30,000 deaths among Americans every year with more than 230,000 new patients in 2004 [1]. Thermal treatment has proven effective for different kinds of tumors including prostate cancer. Hyperthermia therapy raises the temperature of the tumor and a surrounding margin of normal tissue from the normal body temperature of 37°C to 42–45°C for about 30 minutes [2–4]. This type of treatment has had success, in conjunction with radiation therapy, in enhancing the cytotoxic effect of the radiation [5–9]. Ultrasound intracavitary hyperthermia technology is an accepted treatment for prostate cancer.

Previous simulation and design studies of intracavitary ultrasound phased arrays have not considered anatomically realistic human prostate models [10–13]. Preceding

Received November 15, 2005; accepted December 19, 2005.

*Corresponding author. E-mail: eup114@psu.edu

intracavitary ultrasound hyperthermia phased arrays used small cylindrical radiators to conform to the natural contours of large body orifices [14, 15]. Simulations of previous hyperthermia and high intensity focused ultrasound (HIFU) phased arrays were accomplished using the Rayleigh-Sommerfeld integral over a set of a geometrically superimposed point sources [16]. Homogeneous water-like media were used to simulate pressure field distributions of these arrays [10–15, 17]. Such simulations, however, do not capture the interaction of ultrasound with inhomogeneous tissue structures. Accurate modeling of ultrasound wave propagation in inhomogeneous three dimensions (3D) over large length scales has become feasible using the k -space computational method [18, 19]. This method solves the spatial terms of the wave equation by Fourier transformation to the spatial frequency domain; while temporal iterations are performed using a nonstandard finite difference approach using the k - t space propagator (where k represents the spatial frequency domain and t represents the time domain) [18]. In theory, this method requires only two points per wavelength (minimum sampling frequency is twice the frequency of the captured signal for better resolution in the spatial frequency domain (the spatial Nyquist criterion) [20]) for homogeneous media simulations and four points per wavelength for inhomogeneous media [18]. It provides much higher accuracy than the pseudospectral methods, in which the spatial derivatives are evaluated globally by Fourier transformation and wavefields are advanced in time using second order accurate finite differences (leapfrog propagator) [21]. The k -space method maintains its highest accuracy up to a Courant-Friedrichs-Lewy number ($CFL = c_0 \Delta t / \Delta x$, where c_0 is the sound speed; Δt is the temporal step; Δx is the spatial step) of about 0.4 [18]. However, the pseudospectral method rapidly increases in error for CFL numbers above 0.1. For weak scattering media, the k -space method provides similar accuracy for time steps two to three times larger than those required by high order pseudospectral methods [18]. Compared to finite difference computations [22], in which both spatial and temporal second order partial derivatives are solved using second order finite difference computations, the k -space method achieves higher accuracy for a much larger spatial step size. Equivalent accuracy is achieved employing only three points per minimum wavelength using the k -space method compared to 14 points per minimum wavelength for the finite difference equation using the same accuracy criterion. For 3D calculations, this increase in the spatial step reduces the storage requirements for the k -space computations compared to finite difference method by 98% [18].

Specifically, this research uses the k -space computational method to simulate ultrasound wave propagation through an acoustically accurate human prostate model. This technique aids the design and simulation of a hyperthermia planar ultrasound phased array for prostate cancer treatment. The linear phased array described here enables focusing and steering of the acoustic beam in both the propagation and azimuth directions. In the elevation direction, however, the intention is to spread the focal region in the volume that faces the length of the probe by using four stacked phased arrays. Photographic three-dimensional (3D) data from the Visible Human Project[®] (U.S. National Library of Medicine, Bethesda, MD) is used to build the acoustical model of the inhomogeneous medium. The anatomical measurements of the human prostate gland provide essential guide lines for optimal selection of the dimensions of the phased array, while the ultrasound wave propagation simulations predict the pressure volumetric distribution through the prostate model for better heating of both the prostate and the adjacent seminal vesicles. A transducer consisting of four segments of planar ultrasound phased arrays is fabricated using lead zirconate titanate piezo-ceramic for hyperthermia treatment of the prostate gland. The design, simulation, fabrication, exosimetry testing and hyperthermia evaluation of this 4×20 element phased array are presented in this paper.

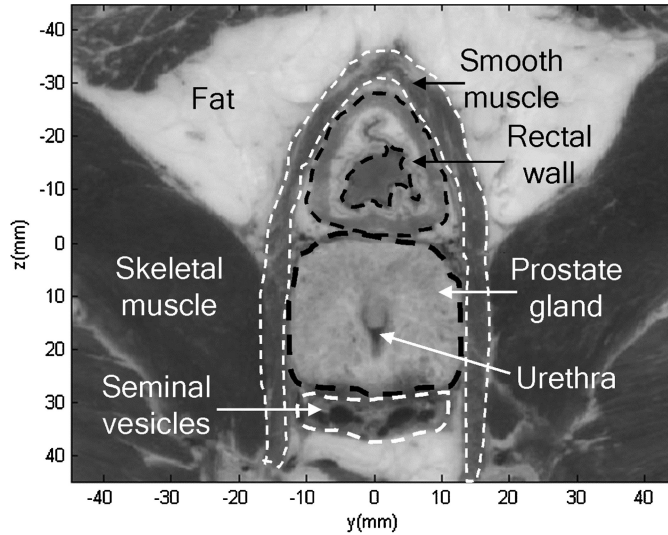


Figure 1. From the Visible Human Project[®], a photographic image of a prostate slice showing a transverse (axial, *yz*-plane) cross section of the prostate gland.

2. Materials and Methods

2.1 Acoustic Modeling, *k*-Space Simulation and Temperature Simulation

Photographic images from the Visible Human Project[®] library were used in constructing a 3D prostate model. Figure 1 shows a transverse (*yz*-plane is the transverse or axial plane; *xy*-plane is the coronal plane; and *xz*-plane is the sagittal plane) photographic slice of this model. It has 89×89 mm dimensions with a 0.25 mm grid size. The prostate gland and the urethral opening are marked and labeled in the figure. The rectum, the prostate gland and the seminal vesicles are surrounded by a sheath of smooth and connective tissues. Surrounding this sheath is a triangular shaped fatty tissue around the rectal wall, while skeletal muscle and connective tissues are neighboring the prostate gland and the seminal vesicles. The original 1 mm distance between adjacent transverse slices of the male subject was unsuitably coarse for simulation of acoustic propagation in the 1.2–1.8 MHz range. To overcome this problem, three extra slices were interpolated from the consecutive 1 mm slices to reduce the distance between neighboring slices to 0.25 mm. The photographic data permitted development of three sets of 3D acoustical data: sound speed variation, density distribution and absorption parameters. Table 1 summarizes the acoustical values from the literature of different tissue types measured at 37°C that were the basis of the model. The fractional fat, connective, glandular and muscle content of each pixel were inferred from the optical parameters [23, 18]. Estimation of the sound speed depended on the fractional content of water, muscle, fat and connective tissues. Mapping the fractional content of water relied on the hue and value of each pixel, while mapping muscle and connective tissues was based on a combination of saturation and value parameters [24]. The mapping of mass density values and absorption parameters relied on empirical linear relations between sound speed and both mass density and absorption parameters. More details are presented elsewhere [23].

Figure 2(a) shows the sound speed mapping of the photographic data which was previously shown in Fig. 1. The color bar relates the sound speed values in m/s to the

Table 1

Acoustical parameters (sound speed, density and absorption) of connective tissue, muscle, fat and water at 37°C and 1.2 MHz. Extrapolation of the absorption value of connective tissue arose from an assumed linear relation between sound speed and absorption for muscle and fat

Tissue type	Sound speed (m/s)	Density (kg/m ³)	Absorption @ 1.2 MHz (dB/m)
Connective	1613*	1120 [†]	103
Muscle	1580 [¶]	1050 [¶]	88.8 [⋈]
Fat	1450 [¶]	950 [¶]	34 [⋈]
Water	1524 [‡]	992 ^ψ	0.3 [‡]

*[26], [†][30], [¶][31], [⋈][32], [‡][33], ^ψ[30].

mapped soft tissue distribution through the slice. Sound speed varies through the soft tissue from 1400 to 1600 m/s. The skeletal muscle tissue, that surrounds the prostate gland, has a sound speed of 1550 m/s. The prostate gland itself is mapped to connective tissue and some fat and muscle tissues. This mapping is consistent with descriptions of the gland consisting of tubular and alveolar tissues imbedded in smooth muscle and connective tissues [25]. The rectal wall translated to muscle (sound speed = 1580 m/s) and fat (sound speed = 1450 m/s) tissues. The connective tissue that surrounds the rectum has a sound speed of 1610 m/s. Figure 2(b) demonstrates density variations that depend on the empirical linear relationship between sound speed and density parameters. The color bar relates density values in kg/m³ to the empirically related soft tissue distribution through the slice. The density varies through the slice from 900 to 1100 kg/m³. Compared to the sound speed map, this figure discriminates each soft tissue distinctly and corresponds well with skeletal muscle, fat, connective tissue and water. Figure 2(c) illustrates the absorption variations mapping of the soft tissue. The color bar relates absorption values in dB/m to the empirically related soft tissue distribution through the slice. The absorption varies from 10 to 100 dB/m for the different soft tissues. The absorption parameters of fat, connective and skeletal muscle tissues match the summarized values in Table 1. Comparing the values of sound speed, density and absorption of various tissues in Fig. 2(a), 2(b) and 2(c), respectively, to the standard values for these soft tissues, this mapping for the whole three-dimensional model provides close agreement to within 1% deviation from the standard reported values in Table 1.

To study the effect of inhomogeneity upon ultrasound waves, the k -space method was used to propagate ultrasound from a spherical source through the acoustical prostate model. The linear acoustic wave equation was used for the simulation:

$$\nabla \cdot \left(\frac{1}{\rho(x, y, z)} \nabla p(x, y, z, t) \right) - \frac{1}{\rho(x, y, z)c^2(x, y, z)} \frac{\partial^2 p(x, y, z, t)}{\partial t^2} = \frac{\alpha(x, y, z)}{\rho(x, y, z)c^2(x, y, z)} \frac{\partial p(x, y, z, t)}{\partial t}$$

where, $\nabla \cdot ()$ is the spatial divergence operator; $\nabla ()$ is the spatial gradient operator; $\rho(x, y, z)$ is the spatially dependent density (kg/m³); $c(x, y, z)$ is the spatially dependent sound speed (m/s); $p(x, y, z, t)$ is the spatially and temporally dependent pressure (Pa); $\alpha(x, y, z)$ is the spatially dependent absorption coefficient (s⁻¹, the absorption in dB/m equals to $20 \times \log_{10}(e) \times \alpha(x, y, z)/(2c_0)$ [23]). All absorption effects (viscous, heat conduction and

internal molecular processes losses) were represented by a single absorption coefficient which was equivalent to the inverse of a spatially dependent relaxation time [26]. The k - t propagator was used to solve for the propagation in the inhomogeneous prostate model after setting both initial and boundary conditions [18]. The dimensions of the model were $64 \times 64 \times 46$ mm with 0.25 mm spatial step size. It was composed of $257 \times 257 \times 185$ discrete points. The temporal step size was $0.082 \mu\text{s}$. A tapered absorption boundary layer, all around the model, was created to prevent wave wrapping from side to side and to prevent reflection of the waves at the boundaries. This layer is mathematically described elsewhere

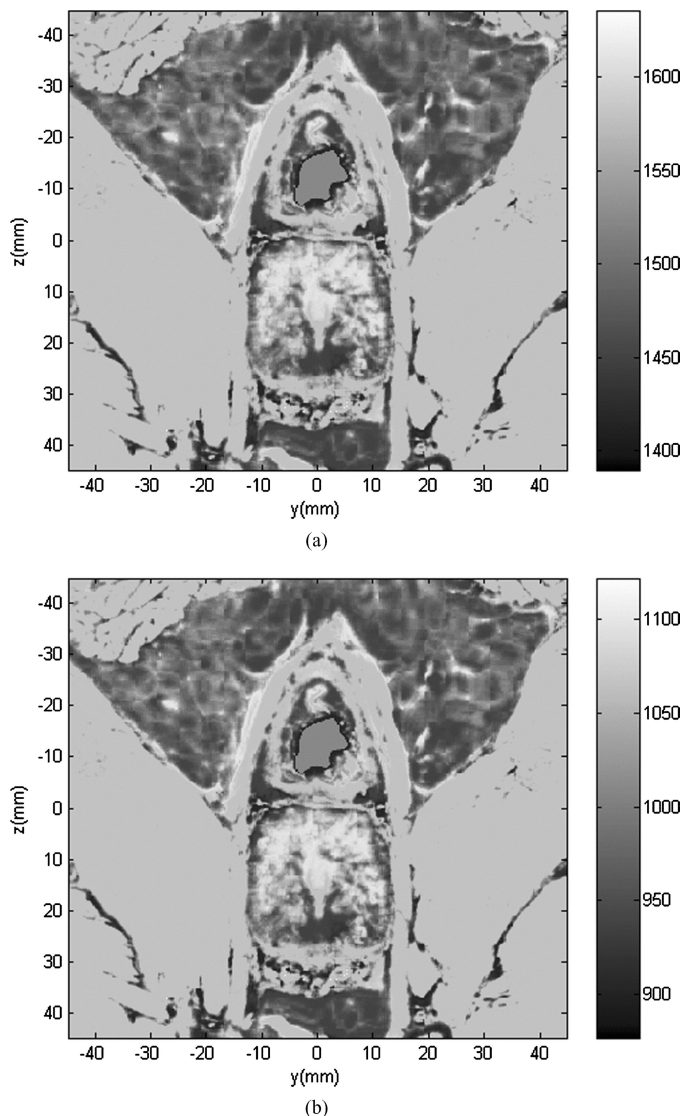


Figure 2. Three sets of acoustical mapping of the photographic data in Fig. 1 are generated for (b) sound speed variations, (c) density values, and (d) absorption parameters. The color bars relate the acoustical values (sound speed (m/s), density (kg/m^3), and absorption (dB/m)) to the soft tissue distribution through the selected slice. (*continued*)

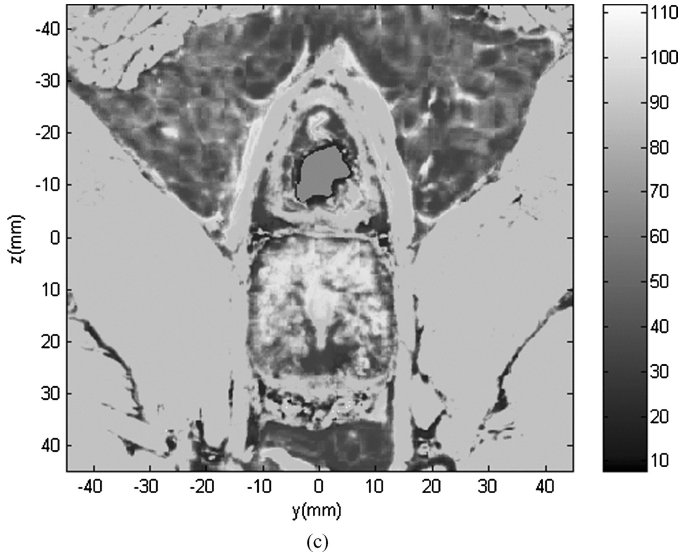


Figure 2. (Continued).

[23]. The spherical source was located in the rectum, five points away from the absorption boundary layer. Pressure variation results through the acoustical model were visualized using gray scale images. Three-dimensional calculations were performed; however, to reduce storage space, the middle slice was selected for image production. Figure 3 shows the log-scale, gray-scale image of spherical wave propagation in the prostate model. It shows the absorption variations through the central slice of the 3D model as a background image with the pressure variations on top of it. An identifiable incident wave leads the scattered wavefield produced from the propagation through the inhomogeneous medium. At the boundaries of the prostate a noticeable reflection and some irregularity of the shape of the wave while crossing the urethra are labeled. This figure validates the k -space method and the acoustical model for investigation of the planar phased array.

Figure 4(a) shows a coronal view (xy -plane) of the 4×20 hyperthermia phased array. It consists of four segments of planar phased arrays; each segment consists of 20 elements with a 1×14 mm sub-element dimension. This arrangement enables focusing and steering of the pressure beam in the propagation and azimuth directions and enables spreading of the focal region in the volume that faces the length of the array. The description of the housing of the phased array in Fig. 4(a), (b), (c), and (d) will be discussed later. The k -space computational method was used to study pressure beam formation and steering of the designed phase array through the prostate model. A single segment of the phased array was incorporated in the acoustical model for simulation purposes. Virtual elements with 1×14 mm dimension were integrated in the simulation. The established grid size of 0.25 mm for the model limited the effective kerf width of the array to this number. Each sub-element added to the overall virtual source that induced pressure to the surrounding media, depending on the acoustical parameters of each point of the model. All points that related to a specific element were driven temporally in a sinusoidal fashion with a 1.2 MHz frequency and a particular phase shift that compensated for its path length to a specific target. To achieve this, a slight modification to the prostate model was made to include the phased array. The modified model included a 20 mm watery region between the location of the active elements and the rectal wall to mimic the proposed water circulation system.

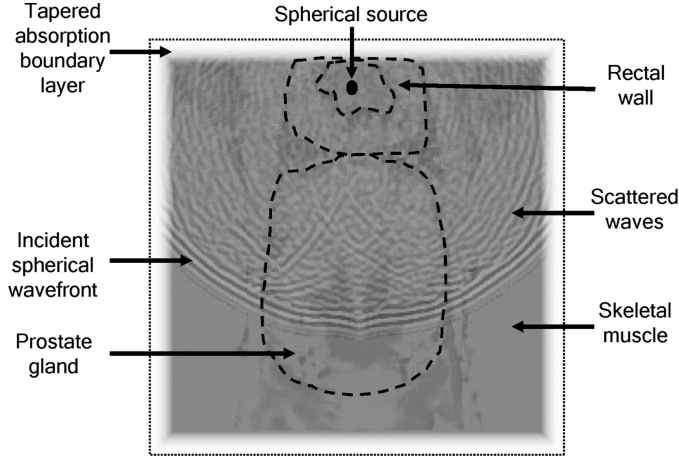


Figure 3. A gray scaled image showing a background layer of the absorption distribution through the middle slice of the 3D prostate model. The tapered absorption boundary layer is shown at the edges with a sharp white color. A black dotted line is surrounding the image to distinguish the absorption layer. A spherically propagated wave is shown on top of this background image showing the wave propagation from left to right through the 3D prostate model. The scattered wave is shown following the three cycles wave that has a frequency of 1.2 MHz. Due to sound speed and density changes through this model the wave front is shown with an irregular shape while propagating through the urethra area.

Temperature simulations were achieved using the bioheat transfer equation [27]:

$$\rho c_t \frac{\partial T(x, t)}{\partial t} = k \left(\frac{\partial^2 T(x, t)}{\partial x^2} \right) - w c_b (T(x, t) - T_a) + q(x)$$

where, $T(x, t)$ is the tissue temperature ($^{\circ}\text{C}$); c_t is the specific heat of the tissue ($3770 \text{ J/kg}^{\circ}\text{C}$); c_b is the specific heat of the blood ($3770 \text{ J/kg}^{\circ}\text{C}$); ρ is the density (998 kg/m^3); k is the thermal conductivity ($0.5 \text{ W/m}^{\circ}\text{C}$); T_a is the arterial blood temperature (37°C); w is the tissue perfusion rate ($8.3 \times 10^{-9} \text{ kg/m}^3\text{s}$); and $q(x)$ is the power deposited locally in the tissue (W/m^3). The square of the acoustic pressure amplitude, which is taken to be proportional to the deposited acoustic power, was extracted along three perpendicular line scans that crossed at the focal volume of the simulated and measured acoustical pressure fields. The temperature rise after two minutes of heating was calculated from the *k*-space and Rayleigh-Sommerfeld simulations and exosimetry measurements along the extracted lines. The temperature was initially set to 37°C in the simulations and then the temperature of the focal point was allowed to increase to 43°C . The Rayleigh-Sommerfeld simulations computed the pressure distribution produced by a single segment of the hyperthermia phased array by summing the pressure contributions of individual simple sources along the extracted lines. The kerf width was 0.12 mm between the elements of the phased array. However, the kerf width for the *k*-space simulations was 0.25 mm . The Rayleigh-Sommerfeld simulations were calculated in water medium without the inclusion of the absorption term.

2.2 Phased Array Fabrication

Lead zirconate titanate (TRS300, TRS Ceramics, State College, PA) ferroelectric material was used for constructing the 4×20 ultrasound phased array. TRS300, being a hard

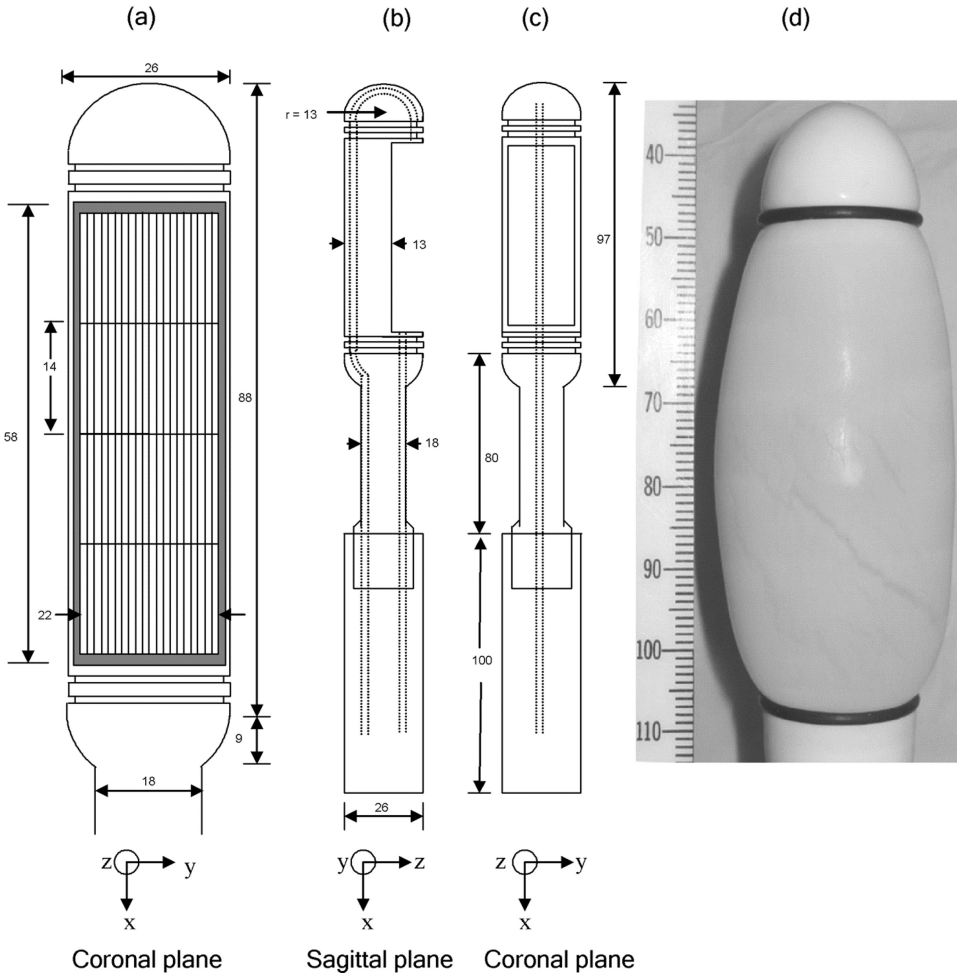


Figure 4. Three diagrams and a photograph showing the transrectal intracavitary ultrasound probe in (a) expanded coronal view (xy -plane), (b) sagittal (xz -plane), (c) coronal (xy -plane), and (d) an actual photograph of the probe with the inflated bolus.

piezo-ceramic, possesses an extremely high mechanical quality factor with the ability to withstand high levels of electrical excitations and mechanical stresses. To increase the efficiency of transmission of acoustical energy in delivering sound energy from the high acoustical impedance of the ceramic to the low acoustical impedance of water or soft tissue, two impedance matching layers were applied onto the ceramic. The choice of these matching layers was aided by design guidelines [28] that gave the desired impedance of quarter wavelength double layers. To construct the double matching layers, Parafilm was used to affix a TRS300 piece to a glass plate. An adhesive primer was poured onto the surface of the ceramic piece. It was then surrounded with an epoxy. A silver bearing, conductive matching layer was poured on top of the ceramic piece. This first layer consisted of a 2:1 epoxy-to-silver mixture of Insulcast 501 (Insulcast Inc., Roseland, NJ) and 2–3 micron silver epoxy (Aldrich Inc., Milwaukee, WI). The whole assembly was centrifuged for 10 minutes and cured overnight. The desired quarter wavelength thickness was obtained

by sanding and lapping the epoxy surface. The second matching layer was made with a similar preparation, but without centrifuging. EPO-TEK 301 part A and part B (Epoxy Technology Inc., Billerica, MA) in a 20:5 mixing ratio created a clear uncured viscous fluid. Another piece of glass spread this mixture on top of the first conductive layer, and appropriate fixtures stabilized the assembly while it cured overnight. After removing the fixtures and the second glass piece, another sanding and lapping process reduced this layer to the required quarter wavelength thickness. Heating the bonding Parafilm wax allowed the separation of the TRS300 piece with its two acoustical matching layers from the glass.

The complete array was formed by dicing the assembly into 80 elements. The dicing cuts were all the way through the thickness of the TRS300 ceramic but not through the matching layers. These cuts were made using a dicing saw (Model 780, K & S-Kulick and Soffa Industries, Willow Grove, PA) with a kerf width of 0.12 mm, the thickness of the cutting blade. Sixty, 28 American Wire Gauge (AWG) miniature magnetic resonance imaging (MRI) compatible coaxial cables (Belden Inc., St. Louis, MI), ten meters long, formed a bundle of cables that connected the elements of the array to an amplifier system. The central two segments of the hyperthermia phased array were electrically connected in parallel. Figure 4(a) shows a coronal view of the diced phased array placed in the specialized Delrin[®] plastic transrectal housing. The actual dimension of each segment is 14 × 22 mm; while the dimension of the whole array is 56 × 22 mm. RHODORSIL[®] V-1022 (Rhodia Inc., Cranbury, NJ) water proof insulation silicone is used to bond and seal the array to its housing. The housing includes groves to contain o-rings that hold the water bolus in place using a latex membrane, a pair of brass tubes to circulate water in front of the array, another pair of brass tubes to circulate air in the cavity behind the array, and a 100 mm hollow cylindrical handle. The diameter of the penetrating cylindrical portion of the probe is 26 mm diameter × 100 mm length including the rounded front and rear. A smaller diameter cylindrical portion follows the penetrating section of the probe with dimensions of 18 mm diameter × 80 mm length. Figures 4(b) and (c) show sagittal and coronal views of the transrectal probe, respectively. The dotted parallel lines show the location of the brass tubes for the water circulation system. The penetrating part, that contains the phased array, is 97 mm length × 26 mm diameter; the following un-penetrating part is 70 mm length × 18 mm diameter. The handle is 100 mm length × 26 mm diameter. Figure 4(d) shows the transrectal probe with its bolus inflated. The water bolus and the circulation system are essential for acoustic coupling between the probe and the tissue surrounding it, and for cooling of the piezoelectric ceramic. A water pump (Cole-Parmer Instrument Company, Barrington, IL) and a temperature controlled bath within the circulation system maintained the temperature and flow of the circulated water.

2.3 *Exposimetry Testing and Hyperthermia Evaluation*

The hyperthermia phased array system was tested using an in-house automated exposimetry system based on the American Institute of Ultrasound in Medicine and National Electrical Manufacturers Association (AIUM/NEMA) guidelines [29]. The array was submerged in an anechoic tank (122 × 51 × 53 cm) filled with degassed distilled water. A needle-type hydrophone (Precision Acoustics Ltd., Dorchest, UK) was placed perpendicular to the face of the transducer to measure pressure field values at discrete points. While focusing the acoustical energy 40 mm away from the face of the transducer, seven scans were acquired for a single phased array. The average values of these scans were compared to *k*-space and Rayleigh-Sommerfeld simulation results.

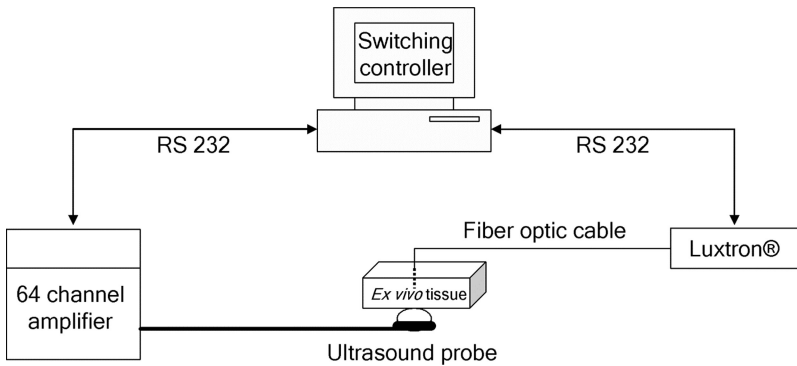


Figure 5. The hyperthermia setup showing the switching controller, the fluoroptic thermometer, the power amplifier, and the transrectal probe.

Ex vivo hyperthermia evaluations of the probe were made using Fleuroptic[®] thermometry and a switching feedback controller. Figure 5 shows the setup for the hyperthermia experiments. A personal computer used as a switching temperature controller was connected via an RS 232 serial port to the digital power amplifier (UDS 2050PA, Advanced Surgical Systems, Inc., Tucson, Arizona) and to the Fleuroptic thermometer system (Luxtron 3100 Fleuroptic thermometer, Luxtron Corp., Mountain View, CA). The ultrasound transrectal probe was coupled to a bovine *ex vivo* sample using an inflated water bolus on top of the face of the array. The transducer was connected to the driving power amplifier. Water hoses were connected to a water pump via a bubble trap chamber and air hoses were connected to an air pump. A 20 gauge needle catheter located the fiber optic thermometer probe inside the *ex vivo* tissue sample in the focal volume of the phased array. Temperature values inside the bovine tissue were read directly from the Luxtron system by the switching controller computer via the RS 232 serial port. Depending on feedback temperature values, the switching controller adjusted the driving power of each ultrasound channel by signaling the power amplifier system on and off. The temperature was made to rise from 37°C to 43°C and was maintained for 30 minutes. For two driving power levels (5 and 10 W), the results of seven experiments were averaged and were plotted including the standard deviation error bars for the period of the experiment using MATLAB[®] software (MathWorks Inc., Natick, MA). These hyperthermia experiments resembled the required clinical thermal dose (43°C for 30 minutes) for cancer treatment purposes.

3. Results

3.1 Simulation Results Using the k-Space Method

Figure 6(a) shows a two-layered gray-scale image of both the normalized pressure squared distribution and the absorption variations for the sagittal central slice of the modified 3D prostate model. The dimensions of this slice are 64 × 64 mm. The white colored layer surrounding the slice represents the tapered absorption boundary layer. It prevents the reflection and wrapping of the ultrasound waves at the boundaries. The phased array is located 5 mm away from the absorbing boundary layer. It is coupled to the rectal wall through the water medium. The pressure squared distribution is represented by the white colored waves on top of the absorption gray-scale distribution. Inhomogeneous tissue composition through the

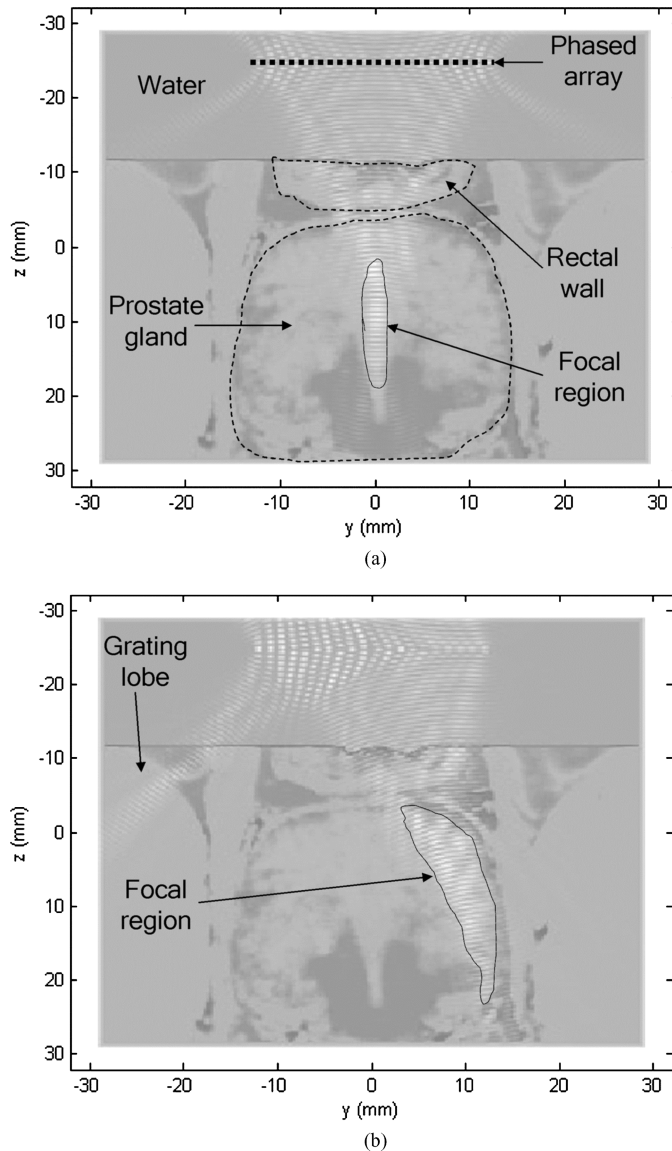


Figure 6. Gray scaled images showing the normalized pressure squared distribution results of a single segment of the hyperthermia phased array using the *k*-space computational method. These results are shown for the central transverse plane of the 3D prostate model. Two-layered gray scale image for the central plane showing a background layer of the absorption distribution and the normalized squared pressure distribution on top of it while focusing (a) axially 40 mm away from the face of the array and (b) focusing off axis at $y = -10$ mm.

rectal wall causes irregularity of the focused beam. The acoustic energy is focused inside the prostate gland 40 mm from the phased array. The phased array, the water medium, the rectal wall, the prostate gland, and the pressure focal region are labeled in the figure. Figure 6(b) shows the same arrangement as in Fig. 6(a) but with steering the focused ultrasound beam towards the boundaries of the prostate gland. The inhomogeneous composition

of the targeted region enhances the distribution of the focal region. Compared to the axial focused beam (Fig. 6(a)), the steered beam is covering larger area. This phenomenon improves the hyperthermia treatment by heating larger volumes at once. The grating lobe levels are -5 dB, -10 dB, -15 dB for selected steering angles of 14.5° , 7.2° and 0.0° , respectively. These angles represent Cartesian focal points of $(x = 0.0$ mm, $y = \pm 10.0$ mm, $z = 40.0$ mm), $(x = 0.0$ mm, $y = \pm 5.0$ mm, $z = 40.0$ mm), and $(x = 0.0$ mm, $y = 0.0$ mm, $z = 40$ mm), respectively.

3.2 Exosimetry Results Compared to Simulation Results

Figure 7(a) shows the normalized pressure distributions of a line that crosses the focal point in the y -direction. The mean exosimetry results are compared to the Rayleigh-Sommerfeld, k -space in water medium, and k -space in prostate model simulations. Compared to simulation results, the exosimetry results show elevated pressure distributions of side lobes (less than -6 dB). These are due to slight misalignment of both the probe and the hydrophone during the exosimetry testing. The measured -3 dB width of the focal volume in the y -direction is 2.0 ± 0.50 mm. Close agreement of exosimetry results in the y -direction compared to simulation results of Rayleigh-Sommerfeld, k -space in water medium and k -space in the prostate model are evident. Figure 7(b) shows another comparison of linear axial scans (z -direction) of the normalized pressure values crossing the focal volume. The k -space simulation in the prostate model shows that the inhomogeneous tissue structure of the rectal wall and the prostate gland cause focusing aberration and elevation of the pressure values (≤ 3 dB) within the nearfield region compared to exosimetry and other simulations. Rapid decrease in the pressure values of the k -space prostate simulation is due to the relatively high absorption values. Figure 2(c) shows that this axial line mostly composed of connective tissue with absorption values of 110 dB/m. Both exosimetry results and k -space water simulation results show good agreement within 9% . Rayleigh-Sommerfeld simulation show deviation of the results compared to the k -space simulations and exosimetry results. This deviation is due to performing the calculations of the pressure values without the inclusion of absorption effects. Table 2 summarizes the -3 dB widths of the focal volume of exosimetry results and the different simulation methods.

Temperature simulation results for two perpendicular lines that cross the focal volume in the y and z directions are shown in Fig. 8. Figure 8(a) shows temperature elevation distribution in the y -direction. Compared to the temperature at the focal point, a negligible temperature increase of the side lobes is noticed for the Rayleigh-Sommerfeld and k -space simulations. The simulated temperature distribution of the extracted exosimetry

Table 2

Summary of the -3 dB distances of focal volume of a single segment of the hyperthermia phased array while focusing axially 40 mm away from the face of the transducer

Type	-3 dB distances of the focal volume (mm)	
	y -direction	z -direction
Exosimetry measurement	2.0 ± 0.50	19.8 ± 0.41
k -space simulation in prostate model	2.0	22.0
k -space simulation in watery medium	2.0	20.0
Rayleigh-Sommerfeld simulation	2.0	28.0

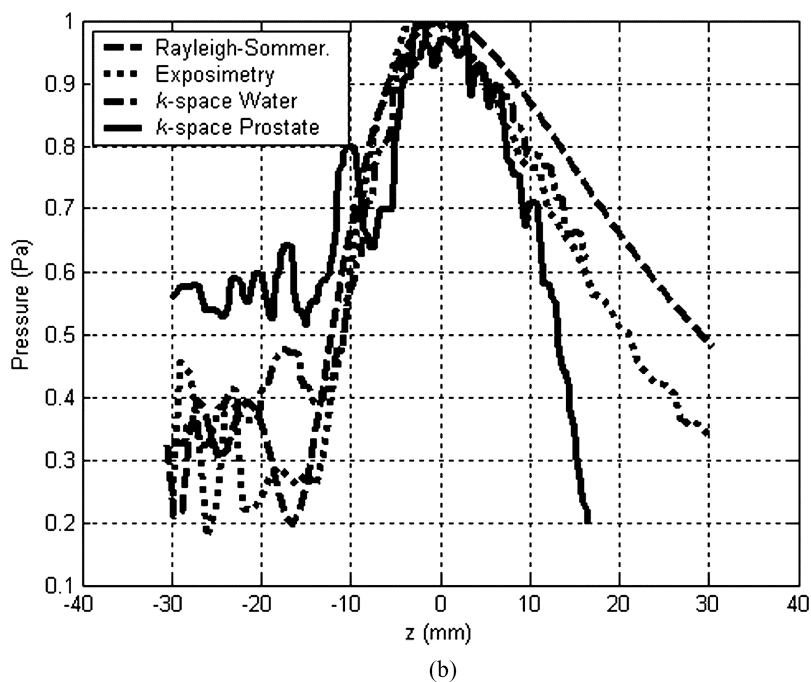
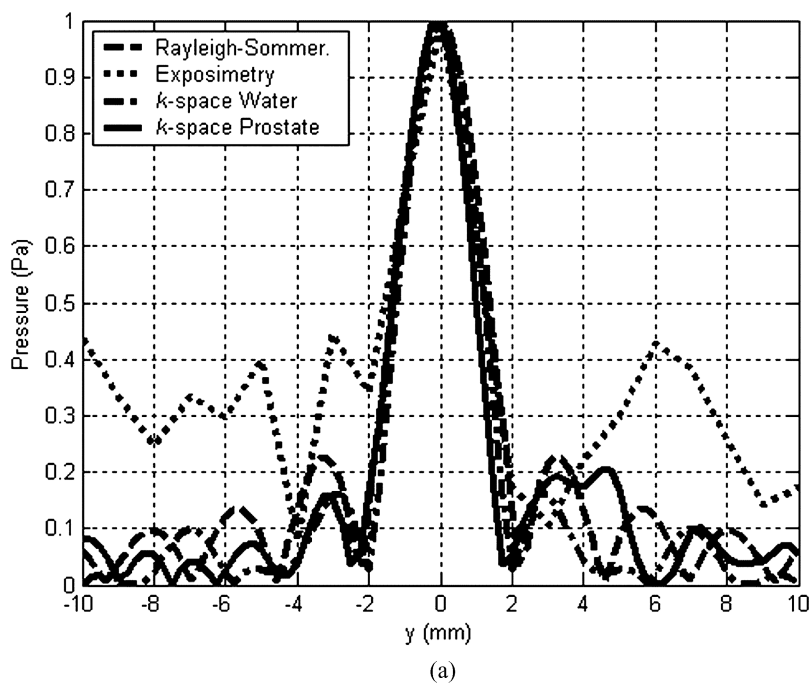


Figure 7. Normalized pressure distribution in linear scans through the focal point in the (a) y -direction and (b) z -direction for results of exposimetry averaged tests, Rayleigh-Sommerfeld simulations, k -space simulations in both water and inhomogeneous prostate media.

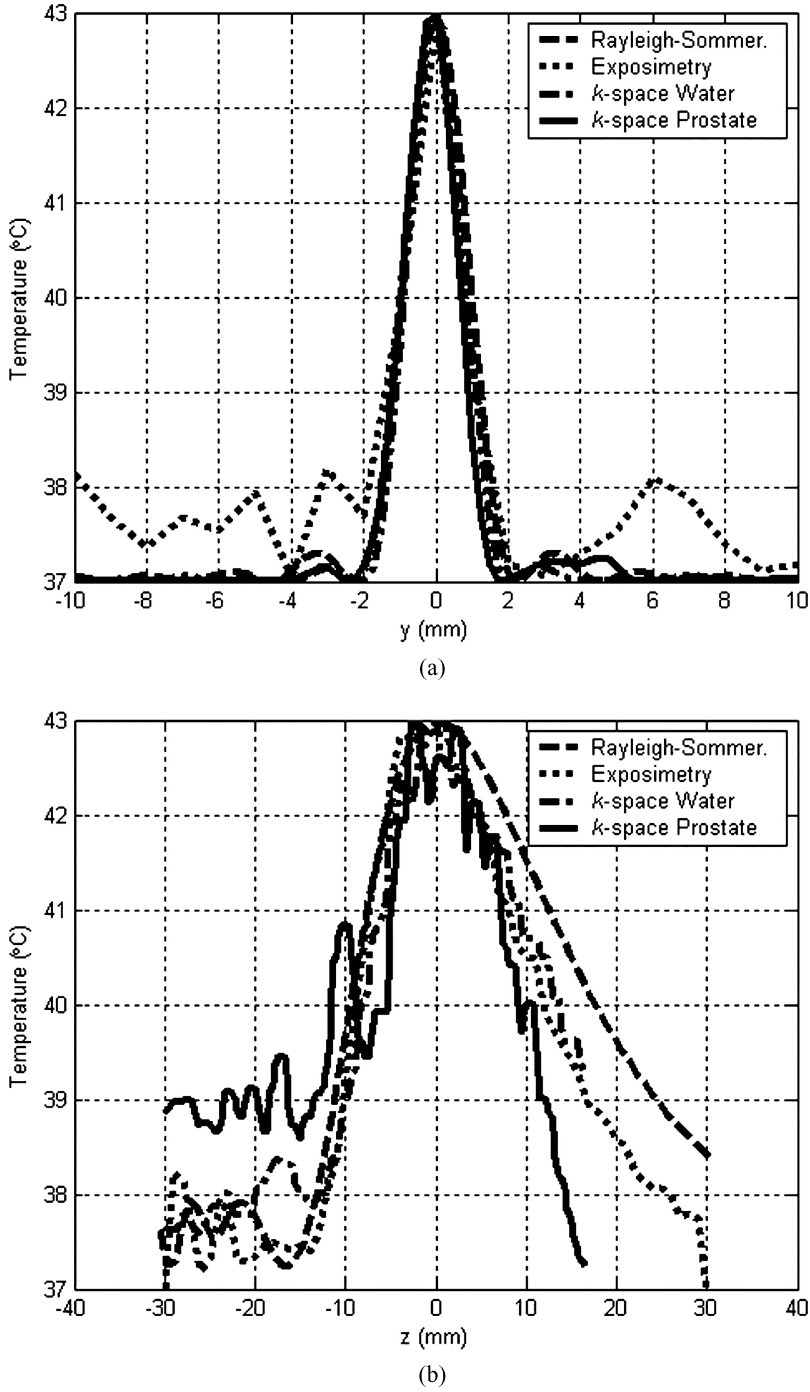


Figure 8. Linear temperature distributions through the focal point for expositometry and simulation results in the (a) y-direction, (b) z-direction.

distribution shows only 1°C increase by the side lobes compared to 6°C at the focal point. Figure 8(b) shows the temperature simulation results in the *z*-direction line. Due to the inhomogeneous composition of the rectal wall and the prostate gland, the temperature of the rectal wall is elevated by 2°C compared to 6°C at the focal point. Homogenous simulations and measured exosimetry results show an increase of 1°C in the nearfield area.

Figure 9(a) shows the *ex vivo* hyperthermia results of the probe using maximum power level of 10 W per element. The temperature is raised from 37°C to 43°C in 7.3 ± 0.4 minutes and maintained steady at $43.1 \pm 0.16^{\circ}\text{C}$ for thirty minutes. The continuous line represents the mean value of seven hyperthermia trials, in which discrete temperature values every two seconds are read from the Luxtron[®] thermometer for thirty minutes. The standard deviation error bars of the hyperthermia trials are plotted on discrete points of 30 seconds intervals, for clarity purposes. Figure 9(b) illustrates another *ex vivo* hyperthermia results using maximum power level of 5 W per element. The rise time is 12.7 ± 1.50 minutes and the steady state temperature is $43.0 \pm 0.04^{\circ}\text{C}$. From the previous results, the rise time is reduced by a factor of two when the power level is increased by the same factor.

4. Discussion

The phased array design presented here is capable of focusing acoustic energy deep inside the prostate gland in the propagation direction and is capable of steering the pressure in the azimuth direction. This design intentionally spreads the focal volume in the elevation direction of the array for better uniform heating in the length of the array. Cascading four individual linear arrays together provides enhanced distribution of heat along the length of the array which in turn helps heating the prostate gland and the adjacent seminal vesicles. The dimensions of each sub-array depend on the size of the prostate gland and the rectum. The transrectal housing reduces patient discomfort by having a smaller, cylindrical-shaped non-penetrating portion that decreases the opening of the anus during the treatment. The diameter of the penetrable part of the probe (26 mm) also guarantees less damage and less discomfort. The length of the penetrable part, which is about 10 cm, can be easily reduced, if desired, by either cascading three 1D arrays together or by reducing the diameter of the spherically shaped front and rear of this part. Reducing the number of sub-arrays will not greatly affect the thermal effectiveness of the therapy since the prostate length is approximately 37 mm in the elevation direction along the axis of the probe. The inclusion of a water circulation system within a latex membrane provides effective coupling to and cooling of the rectal wall. The double-layered acoustical matching layers provide good transmission efficiency and at the same time offer an advantageous mounting method for the diced elements.

Exosimetry and simulations results were compared by measuring the -3dB widths of the produced focal volume. Table 2 summarizes these distances while focusing the energy 40 mm away from the face of the transducer for averaged exosimetry results and different simulation results. These simulations are the *k*-space simulation with the inhomogeneous prostate model, the *k*-space simulation in a watery medium, and the conventional Rayleigh-Sommerfeld simulation method in a homogenous watery medium. Good agreement between exosimetry results and *k*-space simulation results is evident. This agreement emphasizes the importance and the accuracy of the *k*-space method in predicting the pressure wavefields. Comparison of the previously described simulation and exosimetry results is also shown in Fig. 7. This figure plots the linear normalized pressure distribution in the propagation direction through the focal point for exosimetry results and different simulation results. Due to the inhomogeneous composition of the prostate gland, the *k*-space results report pressure level variation at the boundary between the rectum and the glandular tissue.

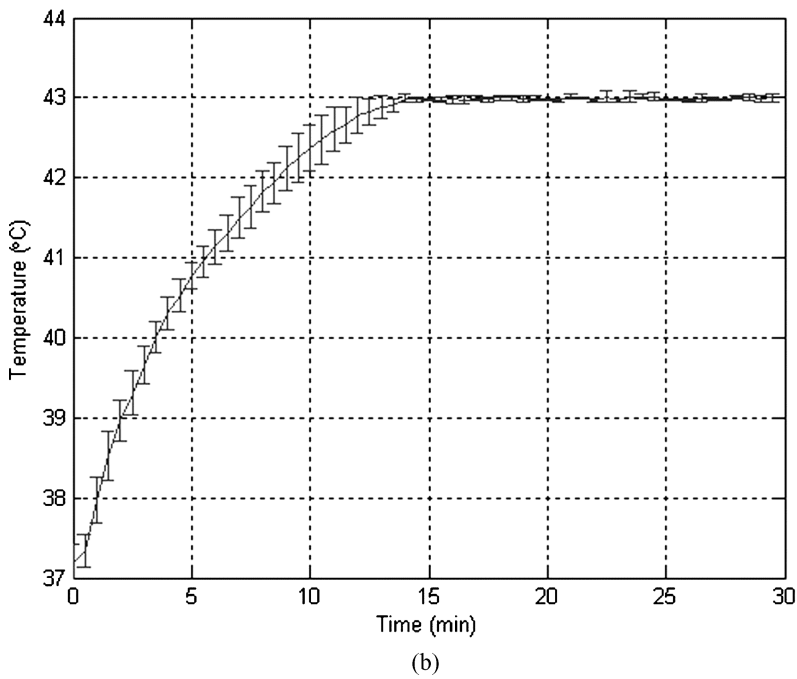
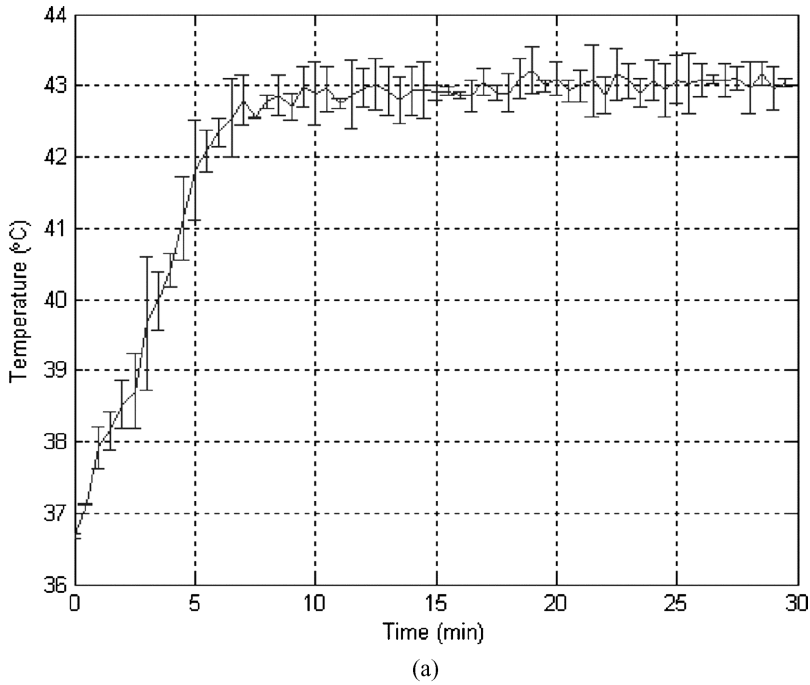


Figure 9. *Ex vivo* controlled hyperthermia results using fleuroptic thermometry for driving electrical powers of (a) 10 W per element and (b) 5 W per element.

Five main goals were achieved in this study. These include the creation of a three-dimensional anatomically accurate acoustical model of the human prostate gland region, the usage of the *k*-space computational method for ultrasound wave propagation through the created model, the design of a novel 4×20 element planar phased ultrasound array which relies on the *k*-space simulations and the acoustic model, the fabrication of an MRI compatible transrectal probe for hyperthermia treatment of prostate cancer, exposimetry testing of the probe utilizing an in-house automated exposimetry system, and *ex vivo* controlled hyperthermia evaluation. Regarding the prostate model, the acoustical conversion of the optical parameters of each pixel of the photographic data proved to be accurate for the whole three dimensional model. It discriminates each soft tissue (fat, muscle, connective and glandular tissues) in good agreement with the standard acoustical reported values. The *k*-space computational method is helpful in simulating ultrasound propagation through coarse-grid, large-scaled, three-dimensional acoustical models. It accounts for tissue inhomogeneity and absorption parameters, and provides a better tool than many conventional computational approaches.

References

1. A. Jemal, R. C. Tiwari, T. Murray, A. Ghafoor, A. Samuels, E. Ward, E. J. Feuer, and M. J. Thun, Cancer statistics 2004. *CA Cancer J. Clin.* **54**, 8–29 (2004).
2. M. Seegenschmiedt and R. Saur, *Interstitial and Intracavitary Thermoradiotherapy*. Berlin: Springer-Verlag (1993).
3. M. Seegenschmiedt, P. Fessenden, and C. Vernon, *Principles and Practices of Thermoradiotherapy and Thermochemotherapy*. Berlin: Springer-Verlag (1995).
4. P. Stauffer, C. Diederich, and M. Seegenschmiedt, *Interstitial Heating Technologies* in M. H. Seegenschmiedt, P. Fessenden, and C. C. Vernon (eds.). *Principles and practices of thermoradiotherapy and thermochemotherapy*. Berlin: Springer-Verlag, 279–320 (1995).
5. W. Dewey, L. Hopwood, S. Sapareto, and L. Gerweck, Cellular response to combinations of hyperthermia and radiation. *Radiation Biology* **123**, 463–479 (1976).
6. P. K. Sneed and T. L. Phillips, Combining hyperthermia and radiation: How beneficial?. *Oncology (Huntingt)* **5**, 99–108 (1991).
7. B. A. Bornstein, P. S. Zouranjian, J. L. Hansen, S. M. Fraser, L. A. Gelwan, and B. A. Teicher, GK: Local hyperthermia, radiation therapy, and chemotherapy in patients with local-regional recurrence of breast carcinoma. *Int. J. Radiat Oncol. Biol. Phys.* **25**, 79–85 (1993).
8. J. Overgaard, G. D. Gonzalez, M. C. Hulshof, G. Arcangeli, O. Dahl, O. Mella, and S. M. Bentzen, Hyperthermia as an adjuvant to radiation therapy of recurrent or metastatic malignant melanoma. A multicentre randomized trial by the European Society for Hyperthermic Oncology. *Int. J. Hyperthermia* **12**, 3–20 (1996).
9. M. Van Vulpen, A. A. C. de Leeuw, B. W. Raaymakers, R. J. A. van Moorselaar, P. Hofman, J. J. W. Lagendijk, and J. J. Battermann, Radiotherapy and hyperthermia in the treatment of patients with locally advanced prostate cancer: Preliminary results. *Bju International* **93**, 36–41 (2004).
10. K. Y. Saleh and N. B. Smith, Two-dimensional ultrasound phased array design for tissue ablation for treatment of benign prostatic hyperplasia. *International Journal of Hyperthermia* **20**, 7–31 (2004).
11. K. Saleh and N. B. Smith, Design and evaluation of a 3×21 element 1.75 dimensional tapered ultrasound phased array for the treatment of prostate disease. *Materials Research Innovations* (2004).
12. L. Curiel, F. Chavier, R. Souchon, A. Birer, and J. Y. Chapelon, 1.5-D high intensity focused ultrasound array for non-invasive prostate cancer surgery. *IEEE Transactions on Ultrasonics Ferroelectrics and Frequency Control* **49**, 231–242 (2002).

13. J. S. Tan, L. A. Frizzell, N. Sanghvi, S. J. Wu, R. Seip, and J. T. Kouzmanoff, Ultrasound phased arrays for prostate treatment. *J. Acoust. Soc. Am.* **109**, 3055–3064 (2001).
14. C. J. Diederich and K. Hynynen, The feasibility of using electrically focused ultrasound arrays to induce deep hyperthermia via body cavities. *IEEE Trans Ultrason Ferroelectr Freq Contr.* **38**, 207–219 (1991).
15. M. T. Buchanan and K. Hynynen, Design and experimental evaluation of an intracavitary ultrasound phased array system for hyperthermia. *IEEE Trans. Biomed. Eng.* **41**, 1178–1187 (1994).
16. J. Zemanek, Beam behavior within the nearfield of a vibrating piston. *J. Acoust. Soc. Am.* **49**, 181–191 (1971).
17. E. B. Hutchinson and K. Hynynen, Intracavitary phased arrays for non-invasive prostate surgery. *IEEE Trans. Ultrason. Ferroelectr. Freq. Contr.* **43**, 1032–1042 (1996).
18. T. D. Mast, L. P. Souriau, D. L. Liu, M. Tabei, A. I. Nachman, and R. C. Waag, A k -space method for large-scale models of wave propagation in tissue. *IEEE Trans. Ultrason. Ferroelectr. Freq. Control* **48**, 341–354 (2001).
19. M. Tabei, T. D. Mast, and R. C. Waag, A k -space method for coupled first-order acoustic propagation equations. *J. Acoust. Soc. Am.* **111**, 53–63 (2002).
20. A. V. Oppenheim, R. W. Schaffer, and J. R. Buck, *Discrete-Time Signal Processing*, 2nd ed. New Jersey: Prentice-Hall, Inc. (1998).
21. D. C. Witte and P. G. Richards, *The Pseudospectral Method for Simulating Wave Propagation*, in Lee D, Cakmak A, and Vichnevetsky R. (eds.). Computational acoustics. New York: North-Holland, 1–18 (1990).
22. E. H. Twizell, *Computational Methods for Partial Differential Equations*. New York: Ellis Horwood Limited (1984).
23. T. D. Mast, Two- and three-dimensional simulations of ultrasonic propagation through human breast tissue. *Acoustics Research Letters Online* **3** (2001).
24. T. D. Mast, Empirical relationships between acoustic parameters in human soft tissues. *Acoustics Research Letters Online* **1**, 37–42 (2000).
25. E. N. Maurieb, *Human Anatomy & Physiology*. 5th ed. New York: Addison Wesley Longman (1999).
26. T. D. Mast, L. M. Hinkelman, L. A. Metlay, M. J. Orr, and R. C. Waag, Simulation of ultrasonic pulse propagation, distortion, and attenuation in the human chest wall. *J. Acoust. Soc. Am.* **106**, 3665–3677 (1999).
27. H. H. Pennes, Analysis of tissue and arterial blood temperatures in the resting human forearm. *Journal of Applied Physiology* **1**, 93–122 (1948).
28. R. E. McKeighen, Design guidelines for medical ultrasonic arrays. SPIE International Symposium on Medical Imaging (1998).
29. AIUM/NEMA: Safety standard for diagnostic for ultrasound equipment. *Journal of Ultrasound in Medicine* **2**, S1–S50 (1983).
30. A. D. Pierce, *Acoustics: An Introduction to Its Physical Principles and Applications* Melville. NY: Acoustical Society of America (1989).
31. I. C. o. R. U. a. M. ICRU, *Tissues Substitutes, Phantoms and Computation Modelling in Medical Ultrasound*. Bethesda: ICRU (1999).
32. I. C. o. R. U. a. M. ICRU, *Tissue Substitutes, Phantoms, and Computational Modelling in Medical Ultrasound*. Bethesda: Maryland Report **61**, (1998).
33. L. Kinsler, A. Frey, A. Coppens, and J. Sanders, *Fundamentals of Acoustics*. New York: Wiley (2000).